Angular insensitive nonreciprocal ultrawide band absorption in plasma-embedded photonic crystals designed with improved particle swarm optimization algorithm

Yi-Han Wang(王奕涵) and Hai-Feng Zhang(章海锋)

Citation: Chin. Phys. B, 2023, 32 (**4**): 044207. DOI: 10.1088/1674-1056/ac8929
Journal homepage: http://cpb.iphy.ac.cn; http://iopscience.iop.org/cpb

What follows is a list of articles you may be interested in

A 3-5 μm broadband YBCO high-temperature superconducting photonic crystal

Gang Liu(刘刚), Yuanhang Li(李远航), Baonan Jia(贾宝楠), Yongpan Gao(高永潘), Lihong Han(韩利红), Pengfei Lu(芦鹏飞), and Haizhi Song(宋海智)
Chin. Phys. B, 2023, 32 (**3**): 034213. DOI: 10.1088/1674-1056/acb760

Topological photonic states in gyromagnetic photonic crystals: Physics, properties, and applications

Jianfeng Chen(陈剑锋) and Zhi-Yuan Li(李志远)
Chin. Phys. B, 2022, 31 (**11**): 114207. DOI: 10.1088/1674-1056/ac92d7

Momentum-space polarization fields in two-dimensional photonic-crystal slabs: Physics and applications

Wen-Zhe Liu(刘文哲), Lei Shi(石磊), Che-Ting Chan(陈子亭), and Jian Zi(资剑)
Chin. Phys. B, 2022, 31 (**10**): 104211. DOI: 10.1088/1674-1056/ac8ce5

Omnidirectional and compact Tamm phonon-polaritons enhanced mid-infrared absorber

Xiaomin Hua(花小敏), Gaige Zheng(郑改革), Fenglin Xian(咸冯林), Dongdong Xu(徐董董), and Shengyao Wang(王升耀)
Chin. Phys. B, 2021, 30 (**8**): 084202. DOI: 10.1088/1674-1056/abe22b

Dynamic modulation in graphene-integrated silicon photonic crystal nanocavity

Long-Pan Wang(汪陇盼), Cheng Ren(任承), De-Zhong Cao(曹德忠), Rui-Jun Lan(兰瑞君), and Feng Kang(康凤)
Chin. Phys. B, 2021, 30 (**6**): 064209. DOI: 10.1088/1674-1056/abda2b

---

Angular insensitive nonreciprocal ultrawide band absorption in plasma-embedded photonic crystals designed with improved particle swarm optimization algorithm

Yi-Han Wang(王奕涵)[1] and Hai-Feng Zhang(章海锋)[2,†]

[1] *Bell Honors School of Nanjing University of Posts and Telecommunication, Nanjing* 210023, *China*
[2] *College of Electronic and Optical Engineering & College of Flexible Electronics, Nanjing University of Posts and Telecommunications, Nanjing* 210023, *China*

(Received 21 April 2022; revised manuscript received 30 June 2022; accepted manuscript online 12 August 2022)

Using an improved particle swarm optimization algorithm (IPSO) to drive a transfer matrix method, a nonreciprocal absorber with an ultrawide absorption bandwidth and angular insensitivity is realized in plasma-embedded photonic crystals arranged in a structure composed of periodic and quasi-periodic sequences on a normalized scale. The effective dielectric function, which determines the absorption of the plasma, is subject to the basic parameters of the plasma, causing the absorption of the proposed absorber to be easily modulated by these parameters. Compared with other quasi-periodic sequences, the Octonacci sequence is superior both in relative bandwidth and absolute bandwidth. Under further optimization using IPSO with 14 parameters set to be optimized, the absorption characteristics of the proposed structure with different numbers of layers of the smallest structure unit N are shown and discussed. IPSO is also used to address angular insensitive nonreciprocal ultrawide bandwidth absorption, and the optimized result shows excellent unidirectional absorbability and angular insensitivity of the proposed structure. The impacts of the sequence number of quasi-periodic sequence M and collision frequency of plasma$_1$ ν_1 to absorption in the angle domain and frequency domain are investigated. Additionally, the impedance match theory and the interference field theory are introduced to express the findings of the algorithm.

Keywords: magnetized plasma photonic crystals, improved particle swarm optimization algorithm, nonreciprocal ultra-wide band absorption, angular insensitivity

PACS: 42.70.Qs, 45.10.Db, 94.30.ct **DOI:** 10.1088/1674-1056/ac8929

1. Introduction

Photonic crystals (PCs) have long been pursued since the leading study of Yablonovitch[1] and John.[2] PCs have the unique qualities of photonic band gaps[3,4] and defect modes.[5,6] These splendid qualities make PCs helpful in designing functional devices, such as PC waveguides,[7] devices used to enhance transmission efficiency and resolution of images,[8] and optical sensors.[9,10] Different metamaterials, such as superconductor[11,12] graphene,[13–15] and plasma[16,17] have been utilized in PCs to strengthen their advantages. Plasma was first used as a unit of PCs by Japanese scholars Hojo and Mase.[18] Since then, studies of plasma PCs (PPCs) have appeared expressing qualities of PPCs or exploring applications of PPCs like reciprocal propagation,[19] unidirectional absorption, and polarization splitting.[20]

To achieve their aims, most existing studies used simulation methods like the transfer matrix[21,22] method (TMM), finite-difference time-domain method[23,24] and neural networks[25] solely, which are accurate in calculation but not ideal for optimization. Topology has also been applied to the structural design of PCs. In this paper, an improved particle swarm optimization algorithm (IPSO) has been utilized to drive a TMM to achieve the objective of optimization. Particle swarm optimization (PSO), originally attributed to Kennedy, Eberhart, and Shi,[26,27] has attracted the attention of scholars because of its robustness, few setting parameters, and fast convergence speed, and has become an important research focus of intelligent evolutionary algorithms. To apply a conventional PSO algorithm to solve problems of PPCs, which are high-dimensional (quality of optimization decreases dramatically)[28] and have intricate local minima that hinder the algorithm from finding the authentic global optimum, an improved algorithm aimed at optimization in PPCs is designed. With the help of IPSO driving the TMM, a nonreciprocal absorber with an ultrawide absorption bandwidth and angular insensitivity (UBAI) is designed. Nonreciprocal absorption is widely used in optoelectronic integration and all-optical communication. A diode based on PC has been designed.[29] In this paper, although the structure proposed is inferior to what Liu and Sen designed[29] in terms of integration, it has better performance in nonreciprocity and large angle ability.

Apart from the result of optimization, which is evident, the influence of the main parameters on a physical level is discussed. The impedance matching theory and interference theory are given in this paper to prove the excellent effect of IPSO. The simulated results in this paper can provide ideas

[†]Corresponding author. E-mail: hanlor@163.com; hanlor@njupt.edu.cn

for designing angular insensitive ultrawide band absorbers or switchable absorption modulators.

2. Model and theory

2.1. Basic plasma theory

Plasma has the characteristic of highly adjustable absorption capacity, owing to the external magnetic field influencing the parameters of plasma. The dielectric function of plasma is calculated in this form, which is anisotropic:[30]

$$\hat{\varepsilon}_{\mathrm{p}}=\begin{pmatrix}\varepsilon_1 & 0 & \mathrm{j}\varepsilon_2\\ 0 & \varepsilon_3 & 0\\ -\mathrm{j}\varepsilon_2 & 0 & \varepsilon_1\end{pmatrix}\begin{cases}\varepsilon_1=1-\dfrac{\omega_{\mathrm{p}}^2(\omega+\mathrm{j}\nu_{\mathrm{c}})}{\omega\left[(\omega+\mathrm{j}\nu_{\mathrm{c}})^2-\omega_{\mathrm{c}}^2\right]},\\ \varepsilon_2=\dfrac{-\omega_{\mathrm{p}}^2\omega_{\mathrm{c}}}{\omega\left[(\omega+\mathrm{j}\nu_{\mathrm{c}})^2-\omega_{\mathrm{c}}^2\right]},\\ \varepsilon_3=1-\dfrac{\omega_{\mathrm{p}}^2}{\omega(\omega+\mathrm{j}\nu_{\mathrm{c}})},\end{cases} \tag{1}$$

where ω_{p} is the plasma frequency, ω_{c} is the cyclotron frequency, and ν_{c} is the collision frequency. These three parameters are basic parameters determining the kind of plasma. ω is the frequency of the incident wave. The determined forms of ω_{p} and ω_{c} are $\omega_{\mathrm{p}}=\left(e^2n_{\mathrm{e}}/\varepsilon_0 m\right)^{1/2}$ and $\omega_{\mathrm{c}}=(eB_0/m)$.

To simplify the process of parameter selection, the determined pattern is not used in parameter optimization; instead, ω_{p} is discussed as a whole, and the numerical values of ω_{c} and ν_{c} are discussed by comparing with ω_{p}. The determined pattern is used to estimate the orders of magnitude of ω_{p} when it comes to parameter optimization.

The effective dielectric constant of plasma is not the same when the incident wave obeys transverse electric (TE) mode or transverse magnetic (TM) mode; the electric field of the former and the magnetic field of the latter are perpendicular to the xz plane. The propagation of the TE wave through the plasma layer is not susceptible to the external magnetic field, so the effective dielectric constant of 1D magnetized PPCs has the same form as that of the unmagnetized ones; in contrast, a TM wave propagating through the plasma layer is highly affected by it.

When the incident wave obeys TE mode, the effective dielectric of plasma can be written as[31]

$$\varepsilon_{\mathrm{TE}}=1-\frac{\omega_{\mathrm{p}}^2}{\omega^2+\mathrm{j}(\nu\omega)}. \tag{2}$$

When the incident wave is under TM mode, the effective dielectric is[31]

$$\varepsilon_{\mathrm{TM}}=\frac{\varepsilon_1^2-\varepsilon_2^2}{\varepsilon_1}=\frac{\left[\omega(\omega+\mathrm{j}\nu_{\mathrm{c}})-\omega_{\mathrm{p}}^2\right]^2-\omega^2\omega_{\mathrm{c}}^2}{\omega^2\left[(\omega+\mathrm{j}\nu_{\mathrm{c}})^2-\omega_{\mathrm{c}}^2\right]-\omega\omega_{\mathrm{p}}^2(\omega+\mathrm{j}\nu_{\mathrm{c}})}. \tag{3}$$

2.2. Calculation method

2.2.1. Transfer matrix method

The TMM is aimed at solving the transmission characteristics and dispersion relations of PCs by deriving the iterative equations of the electric field and magnetic field according to their continuous boundary conditions based on Maxwell's equations.

For the i-th single layer of the proposed 1D magnetized PPCs, the recursive matrix equation can be written as

$$\begin{pmatrix}E_i\\ H_i\end{pmatrix}=\boldsymbol{M}\begin{pmatrix}E_{i+1}\\ H_{i+1}\end{pmatrix}. \tag{4}$$

Under TE mode, the transfer matrix of the normal dielectric layer and the plasma layer is

$$\boldsymbol{M}_i^{\mathrm{TE}}=\begin{pmatrix}\cos(k_{iz}d_i) & -\frac{\mathrm{j}}{\eta_i^{\mathrm{TE}}}\sin(k_{iz}d_i)\\ -\mathrm{j}\eta_i^{\mathrm{TE}}\sin(k_{iz}d_i) & \cos(k_{iz}d_i)\end{pmatrix}, \tag{5}$$

where $k_{iz}=k_i\cos\theta$, $k_i=\sqrt{\varepsilon_i}\omega/c$, $\eta_i^{\mathrm{TE}}=\sqrt{\varepsilon_0/\mu_0}\sqrt{\varepsilon_i}\cos\theta_i$, d_i represents the thickness of the i-th layer, and ε_i represents the equivalent permittivity of the i-th layer.

Under TM mode, the transfer matrix of the normal dielectric layer and plasma layer can be written as

$$\begin{aligned}
&\boldsymbol{M}_i^{\mathrm{TM}}(\mathrm{norm})=\begin{pmatrix}\cos(k_{iz}d_i) & -\frac{\mathrm{j}}{\eta_i^{\mathrm{TM}}}\sin(k_{iz}d_i)\\ -\mathrm{j}\eta_i^{\mathrm{TM}}\sin(k_{iz}d_i) & \cos(k_{iz}d_i)\end{pmatrix},\\
&\boldsymbol{M}_i^{\mathrm{TM}}(\mathrm{plasma})=\begin{pmatrix}m_{11} & m_{12}\\ m_{21} & m_{22}\end{pmatrix},\\
&m_{11}=\cos(k_{iz}a)+\frac{k_{ix}\varepsilon_2}{k_{iz}\varepsilon_1}\sin(k_{iz}a),\\
&m_{22}=\cos(k_{iz}a)-\frac{k_{ix}\varepsilon_2}{k_{iz}\varepsilon_1}\sin(k_{iz}a),\\
&m_{21}=-\mathrm{j}\eta_i^{\mathrm{TM}}\sin(k_{iz}a),\\
&m_{12}=-\frac{\mathrm{j}}{\eta_i^{\mathrm{TM}}}\left[1+\left(\frac{k_{ix}\varepsilon_2}{k_{iz}\varepsilon_1}\right)^2\right]\sin(k_{iz}a),
\end{aligned} \tag{6}$$

where k_{iz} and d_i share the same formulas and meanings as those shown in formula (5). $\eta_i^{\mathrm{TM}}=\sqrt{\varepsilon_0/\mu_0}\sqrt{\varepsilon}_i/\cos\theta_i$.

In the situations of both TE and TM mode, θ_i represents the angle between the direction of propagation and the z axis in the i-th layer. According to Snell's refraction law, $\theta_i=\arcsin(n_0\sin(\theta_0)/n_i)$, in which n_0 is the environmental refractive index, n_i is the refractive index of the i-th layer ($n_i=\sqrt{\varepsilon_i}$), and θ_0 is the angle of incidence of the wave.

The whole structure is composed of many layers obeying the same recursive matrix equation, so the matrix of the whole can be expressed as follows iteratively:

$$\boldsymbol{M}=\prod_{j=1}^{N}\boldsymbol{M}_j=\begin{pmatrix}M_{11} & M_{12}\\ M_{21} & M_{22}\end{pmatrix}. \tag{7}$$

The reflection coefficient r and the transmission coefficient t can be expressed as

$$r = \frac{(M_{11} + M_{12}\eta_{N+1})\,\eta_0 - M_{21} - M_{22}\eta_{N+1}}{(M_{11} + M_{12}\eta_{N+1})\,\eta_0 + M_{21} + M_{22}\eta_{N+1}}, \tag{8}$$

$$t = \frac{2\eta_0}{(M_{11} + M_{12}\eta_{N+1})\,\eta_0 + M_{21} + M_{22}\eta_{N+1}}. \tag{9}$$

The reflectance R, transmittance T and absorptance A are $R = r \cdot r^*$, $T = t \cdot t^*$, and $A = 1 - T - R$, respectively.

2.2.2. Improved particle swarm optimization algorithm

The number of parameters to be optimized is D, which is also the dimension of space that all the particles lay in. The number of particles is M. The coordinates of particles in D-dimensional space are the present values of the parameters to be optimized, and the value will be tuned to gain the best objective function like particles seeking the best appropriate place. Figure 1 shows the algorithm process.

The location and vector of the n-th particle can be written as

$$\begin{aligned} &\boldsymbol{X}(n) = (x^1(n), x^2(n), \ldots, x^D(n))^{\mathrm{T}}, \quad n = 1, 2, \ldots, M, \\ &\boldsymbol{V}(n) = (v^1(n), v^2(n), \ldots, v^D(n))^{\mathrm{T}}, \quad n = 1, 2, \ldots, M. \end{aligned} \tag{10}$$

Every particle adjusts its vector according to individual optimum position $\boldsymbol{P}_{\mathrm{indi}}(n)$ and group optimum position $\boldsymbol{P}_{\mathrm{gro}}$,

$$\boldsymbol{P}_{\mathrm{indi}}(n) = (p^1_{\mathrm{indi}}(n), p^2_{\mathrm{indi}}(n), \ldots, p^D_{\mathrm{indi}}(n)), \tag{11}$$

which means the individual optimum position of the n-th particle

$$\boldsymbol{P}_{\mathrm{gro}}(n) = (p^1_{\mathrm{gro}}(n), p^2_{\mathrm{gro}}(n), \ldots, p^D_{\mathrm{gro}}(n)), \tag{12}$$

which is the most adaptive particle's location from the first generation to the present generation.

The formula for updating the particles' location and vector is

$$\begin{aligned} &\boldsymbol{X}_{k+1}(n) = \boldsymbol{X}_k(n) + \boldsymbol{V}_k(n), \\ &\boldsymbol{V}_{k+1}(n+1) = u\boldsymbol{V}_k(n) + c_1 \mathrm{rand}\,(\boldsymbol{P}_{\mathrm{indi}}(n) - \boldsymbol{X}_k(n)) \\ &\qquad\qquad + c_2 \mathrm{rand}\left(\boldsymbol{P}_{\mathrm{gro}}(n) - \boldsymbol{X}_k(n)\right), \\ &n = 1, 2, \ldots, M, \quad k = 0, 1, 2, \ldots, G. \end{aligned} \tag{13}$$

In this formula, u is the inertia factor, c_1 and c_2 are the studying factors, and they reflect the degree to which a particle is influenced by itself and the group respectively. In view of the problem of 1D magnetized PPCs to be addressed whose dimension is comparably high and whose objective function has plenty of local maximum, the values of u and c_1, c_2 will significantly influence the efficiency or even correctness of the algorithm. As the ordinal of generation rises, the values of u and c_1 and c_2 can be written as

$$\begin{aligned} &u = u_{\mathrm{en}} + \frac{(u_{\mathrm{be}} - u_{\mathrm{en}})(G - \mathrm{gen})}{G}, \\ &\begin{cases} c_1 = c_{1\mathrm{be}} + (c_{1\mathrm{en}} - c_{1\mathrm{be}})\dfrac{\mathrm{gen}^2}{G^2}, \\ c_2 = c_{2\mathrm{en}} + (c_{2\mathrm{en}} - c_{2\mathrm{be}})\dfrac{\mathrm{gen}^2}{G^2}, \end{cases} \end{aligned} \tag{14}$$

where gen means current iteration time, G means total iteration time, and u_{be}, u_{en} and $c_{1\mathrm{be}}$, $c_{1\mathrm{en}}$ and $c_{2\mathrm{be}}$, $c_{2\mathrm{en}}$ mean the initial value and stop value of u and c_1 and c_2, respectively. At the beginning of iteration, comparably large values of u and c_1 make sure the algorithm avoids being trapped in a local maximum,while at the end of iteration, comparably small values of u and c_1 and a comparably large value of c_2 give a chance for the algorithm to seek the most accurate global maximum and aid the convergence of the sequence of generation.

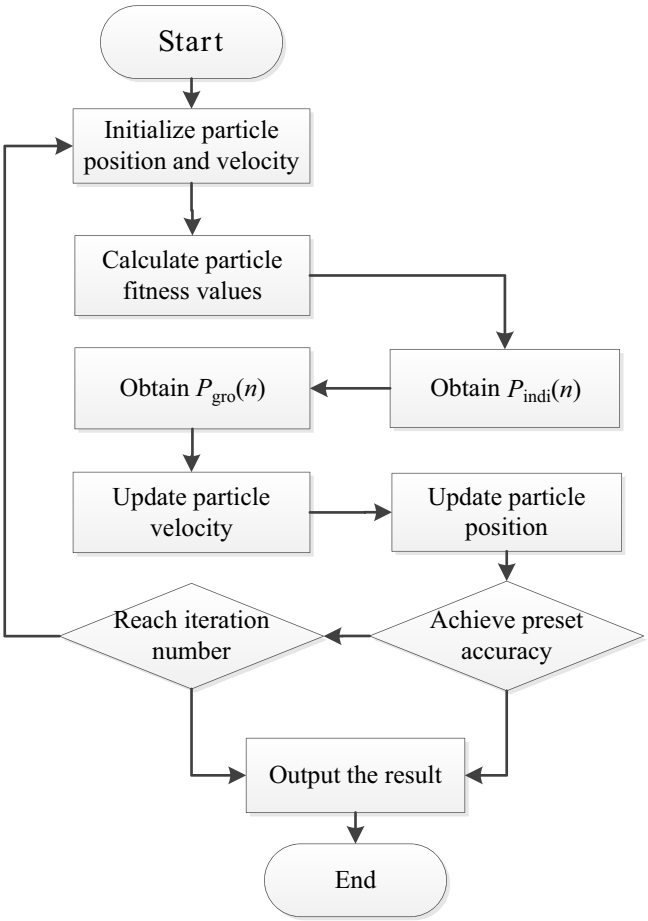

Fig. 1. Algorithm process of IPSO.

2.3. Schematic structure of PPCs and selection of quasi-periodic sequence

A schematic of the proposed PPCs is shown in Fig. 2, as well as the coordinate axis and schematics of the TM and TE waves. The environment is air. The positive direction along the z axis is forward propagation and the negative direction is backward propagation. Observing along the z axis,

the part near the origin is periodic structure $\{AP_AB\}^N$ and the part far from the origin is quasi-periodic structure (Octonacci, Fibonacci, Thue–Morse). The periodic structure and quasi-periodic structure are placed in different magnetic fields B_1 and B_2, respectively, which have the same magnetic field direction but are different in value. This method of two magnetic fields can make sure plasma$_1$ and plasma$_2$ work in their own work zones to produce excellent results. The target is to find the best structure and parameters. There are four kinds of quasi-periodic sequences to choose from

(i) Octonacci sequence:

$$\begin{cases} \mathrm{Oct}_M = \mathrm{Oct}_{M-1}\mathrm{Oct}_{M-2}\mathrm{Oct}_{M-1}, \\ \mathrm{Oct}_1 = \{P_BCP_B\}, \ \ \mathrm{Oct}_0 = \{CP_BC\}; \end{cases}$$

(ii) Fibonacci sequence:

$$\begin{cases} \mathrm{Fib}_M = \mathrm{Fib}_{M-1}, \mathrm{Fib}_{M-2} (M > 1), \\ \mathrm{Fib}_1 = \{P_BCP_B\}, \ \ \mathrm{Fib}_0 = \{CP_BC\}; \end{cases}$$

(iii) Thue–Morse sequence: '0' in the n-th item becomes '01' in the $(n+1)$-th item and '1' becomes '10', where "1" represents $\{P_BCP_B\}$ and "0" represents $\{CP_BC\}$.

To explore the effect of different sequences on absorption characteristics, the amounts of the smallest unit of these four different sequences (structure$\{P_2CP_2\}$ or $\{CP_2C\}$) are similar. We choose Oct_4, Fib_7, Thu_5. Utilizing IPSO, the optimal results of four different sequences are calculated after preliminary optimization.

Figures 3(a)–3(b) shows the results of different sequences. The incident angle is 0°. The absolute bandwidths of the periodic sequence, Thue–Morse sequence, Fibonacci sequence, and Octonacci sequence are 0.68 $(\omega d/2\pi c)$, 1.25 $(\omega d/2\pi c)$, 1.75 $(\omega d/2\pi c)$, and 2.05 $(\omega d/2\pi c)$, respectively. The relative bandwidths of the four sequences are 0.369, 0.549, 1.42, and 1.44, respectively. It is obvious that Octonacci is the best one both in absolute and relative bandwidth.

Comparison of the results of MATLAB and fullwave simulation are shown in Fig. 4, where the results are totally the same. The parameters of the tested plasma layer, which plays a crucial role in the PPC structure proposed, are $\omega_p = 1.8850 \times 10^{12}$, $\omega_c = 1.1310 \times 10^{12}$, $\nu = 1.1310 \times 10^{11}$, and $d = 1$ μm. These results can strongly prove the correctness of the model.

The root of the perfect absorption is an excellent impedance match between the whole structure and the environment. The normalized surface impedance can be expressed by

$$\frac{Z_{\mathrm{eff}}}{Z_0} = z_{\mathrm{r,eff}} + \mathrm{j}z_{\mathrm{i,eff}} = \frac{1+r}{1-r}, \tag{15}$$

where Z_{eff} means the effective surface impedance of the proposed structure and Z_0 means the wave impedance in a vacuum, $Z_0 = |E_0|/|H_0| = \sqrt{\mu_0/\varepsilon_0}$. When the normalized effective surface impedance is close to 1, it represents that the effective impedance of the structure matches well with that of the environment, so the reflection coefficient r is close to 0, which means that reflectance is almost negligible and the electromagnetic energy is ideally restricted in the structure, thus leading to perfect absorption effects. As shown in Fig. 3(c), the real component of Z_{eff} of the Octonacci sequence in forward propagation is around 1 and the imaginary part of that is around 0, which means the complex numerical of Z_{eff} is fluctuating around $1 + j_0$, which realizes the impedance match in this direction.

Comparing Fig. 3(c) with Fig. 3(a), taking the Octonacci sequence for instance, it is found that the distance of the complex numerical of Z_{eff} and $1 + j_0$ is tightly related to absorption of the Octonacci sequence. The distance of Z_{eff} and $1 + j_0$ is plotted in Fig. 3(a); it is obvious that when the distance is close to zero, the absorption is higher, and vice versa. The fluctuation of absorption is sensitive to changes in distance as shown in Fig. 3(a), which proves the rationality of the theory of impedance matching.

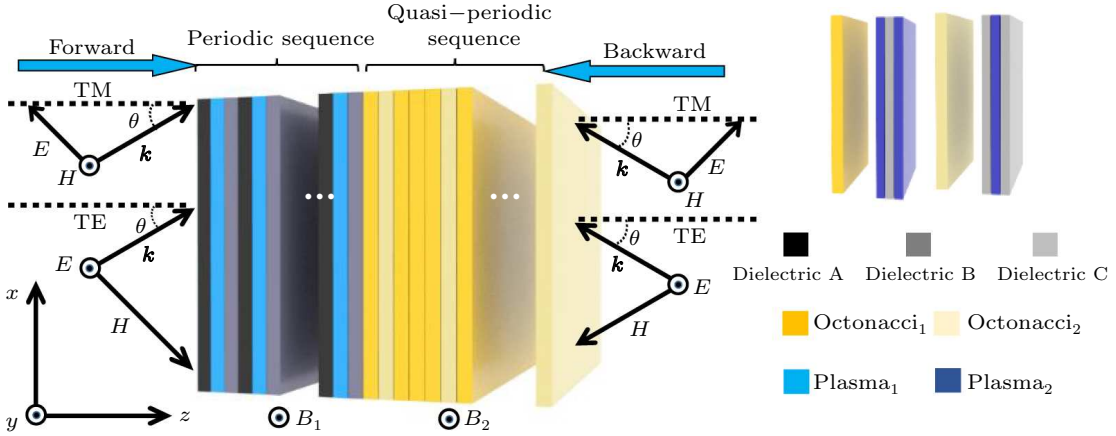

Fig. 2. Schematic illustration of PPC composed of periodic sequence and quasi-periodic sequence.

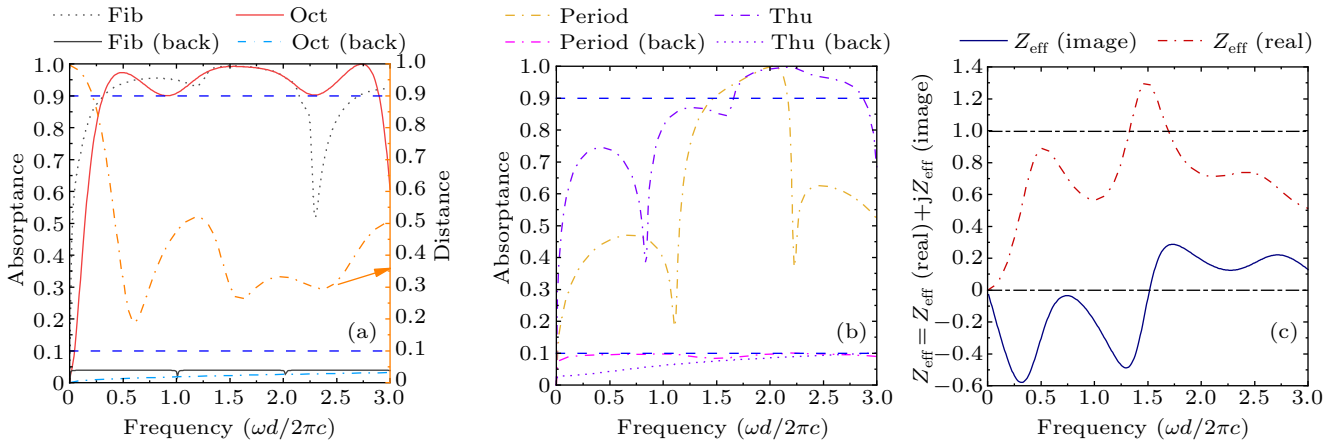

Fig. 3. Results of different sequences and impedance matching of Octonacci sequence. Absorptance of forward and backward propagation of (a) Fibonacci and Octonacci sequence, (b) periodic sequence and Thue–Morse sequence. (c) Real part and imaginary part of normalized surface impedance. Orange dot-dashed curve in (a) describes distance of the complex value of normalized surface impedance and $1 + j_0$.

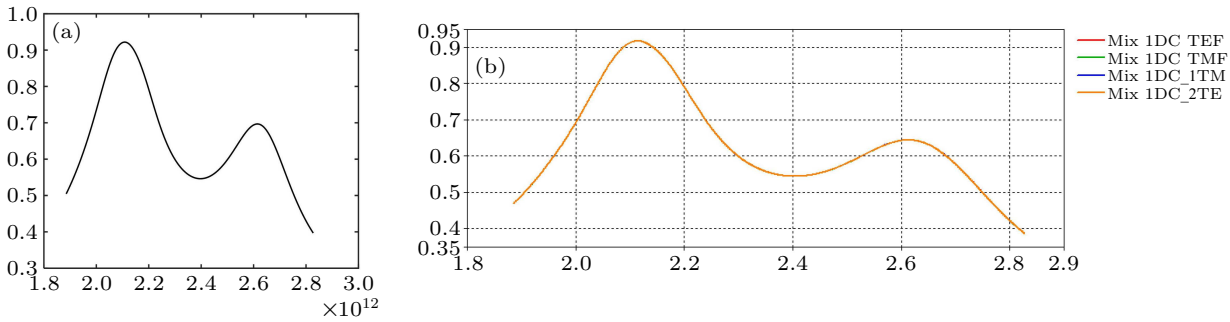

Fig. 4. Calculation results by TMM with MATLAB (a) and the result of fullwave simulation (b) with $\omega_{\rm p} = 1.8850 \times 10^{12}$, $\omega_{\rm c} = 1.1310 \times 10^{12}$, $\nu = 1.1310 \times 10^{11}$, $d = 1$ μm.

3. Results and discussion

3.1. Influences of basic parameters of plasma

To have an immediate concept of basic parameters, diagrams of absorption of plasma, the real part of ε_1 and the imaginary part of ε_2 when three basic parameters take different values under TM mode are shown in Fig. 5.

Diagrams of the absorption characteristics of a single unit of plasma together with the real part of ε_1 and imaginary part of ε_2 with different plasma frequencies of $\omega_{\rm p} = 0.5$, 2, 4, 6, 8, 10 (unit: $\pi c/d$) are shown in Figs. 5(a)–5(c). The specific parameters are $\omega_{\rm c} = 1\omega_{\rm p}$ and $\nu = 0.5\omega_{\rm p}$. When $\omega_{\rm p}$ increases, the extreme point of absorptance and $\mathrm{Re}(\varepsilon_1)$ all shift to higher frequency. The extreme point of absorptance and that of $\mathrm{Re}(\varepsilon_1)$ are highly consistent, while the consistency of the maximum point of absorptance and that of $\mathrm{Im}(\varepsilon_2)$ are not so good: at low frequency, the maximum point of absorptance and $\mathrm{Im}(\varepsilon_2)$ are comparably consistent, but when the frequency becomes higher, the difference increases although they still have a positive correlation. When $\omega_{\rm p}$ increases, the maximum value of absorptance of the plasma grows, and when $\omega_{\rm p}$ increases to $4\pi c/d$ or more, the maximum value of absorptance remains at 1. The bandwidth for which absorptance is higher than 0.9 (absorptance bandwidth) becomes larger when $\omega_{\rm p}$ increases. This shows that the plasma frequency can significantly influence the absorbing properties of the magnetized plasma both in absorption frequency and absorptance.

Figures 5(d)–5(f) show diagrams of the absorption characteristics of a single unit of plasma together with the real part of ε_1 and imaginary part of ε_2 with different plasma cyclotron frequencies of $\omega_{\rm c} = 0.5$, 0.7, 0.9, 1.1, 1.3, 1.5 (unit: $\omega_{\rm p}$). The specific parameters are $\omega_{\rm p} = 2\pi c/d$, $\nu = 0.2\omega_{\rm p}$. When $\omega_{\rm c}$ increases, the extreme point of absorptance, $\mathrm{Re}(\varepsilon_1)$ and $\mathrm{Im}(\varepsilon_2)$ all shift to higher frequency. At low frequency, the maximum point of absorptance and $\mathrm{Re}(\varepsilon_1)$ are positively correlated but not the same, and so are the maximum point of absorptance and $\mathrm{Im}(\varepsilon_2)$. When the frequency becomes higher, the difference between the maximum point of absorptance and $\mathrm{Re}(\varepsilon_1)$ (or $\mathrm{Im}(\varepsilon_2)$) is increasingly small. When $\omega_{\rm c} > 1$, the maximum points of absorptance and $\mathrm{Re}(\varepsilon_1)$ (or $\mathrm{Im}(\varepsilon_2)$) are almost the same. When $\omega_{\rm c}$ increases, the maximum value of absorptance stays almost constant at about 0.95. This means that plasma cyclotron frequencies can prominently affect absorption frequency without changing the maximum absorptance.

Figures 5(g)–5(i) show diagrams of the absorption characteristics of a single unit of plasma together with the real part of ε_1 and imaginary part of ε_2 with different collision frequencies of $\nu = 0.05$, 0.1, 0.3, 0.5, 0.7, 0.9 (unit: $\omega_{\rm p}$). The max-

imum point of absorptance, $\mathrm{Re}(\varepsilon_1)$ and $\mathrm{Im}(\varepsilon_2)$ are the same and remain constant when v increases. When v increases, the maximum value of absorptance and the absorption bandwidth increase while the maximum values of $\mathrm{Re}(\varepsilon_1)$ and $\mathrm{Im}(\varepsilon_2)$ decrease. This means that the collision frequency can largely influence the maximum absorptance and absorption bandwidth without changing the absorption frequency.

It can be concluded that v significantly influences the absorptance bandwidth without shifting the frequency point, ω_c has an impact on the frequency point but little impact on bandwidth, and ω_p is related to both absorption bandwidth and absorption frequency. These finding will provide guidance for numeral parameter selection on a physical level together with impedance matching theory.

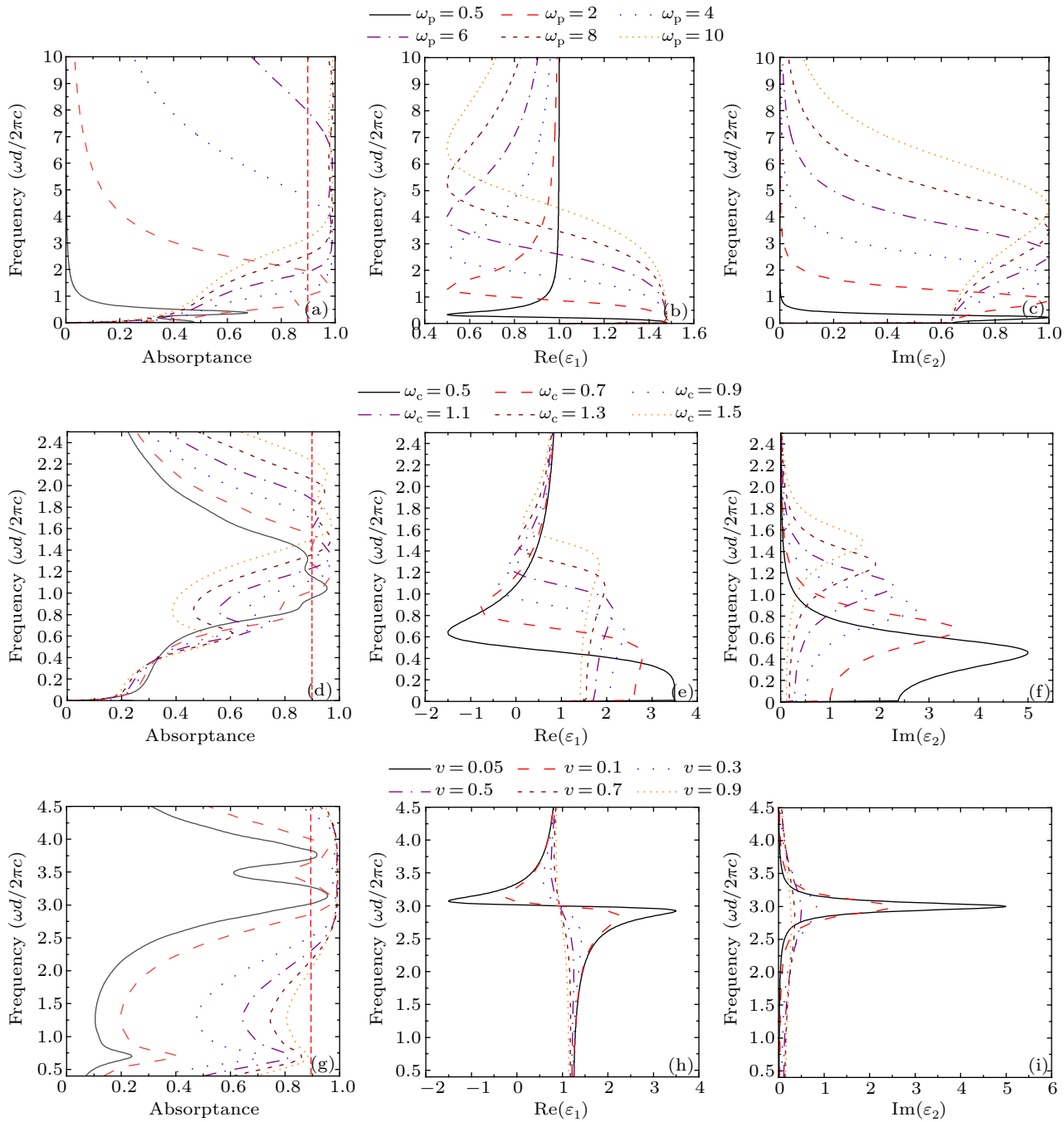

Fig. 5. Comparison of diagrams of absorptance of plasma, real part of ε_1 and imaginary part of ε_2 with different values of ω_p [(a)–(c)], ω_c [(d)–(f)], v [(g)–(i)].

3.2. Ultrawide band absorption of Octonacci sequence

Once the optimal sequence is determined, the rest of the optimization involves determining the values of all the parameters shown in Table 1. Subscripts A, B, and C mean $\mathrm{dielectric_A}$, $\mathrm{dielectric_B}$, and $\mathrm{dielectric_C}$ respectively. Subscripts P_1 and P_2 mean $\mathrm{plasma_1}$ and $\mathrm{plasma_2}$ respectively. Utilizing IPSO, supplemented by impedance matching theory and the intuitive influence of the three basic parameters of

plasma discussed in Subsection 3.1, the best choices of parameter values against different objective functions are calculated successfully. We notice that for the basic parameters of the plasma, the frequencies are all normalized to scale by $d = d_{\mathrm{p1}}$. This means that this paper deals with an abstract model with parameters proportional to each other, and that if one needs to deal with some problems in some particular spectrum or length, the only thing one needs to do is to change d and all the results stay the same.

Table 1. All parameters to be optimized.

Parameters to be optimized					
$d = d_{\mathrm{p1}}$					
Parameter	Unit	Range	Parameter	Unit	Range
ω_{P1}	$\pi c/d$	0–2	ω_{P2}	$\pi c/d$	0–2
ω_{C1}	ω_{P1}	0–2	ω_{C2}	ω_{P2}	0–2
ν_1	ω_{P}	0.05–1	ν_2	ω_{P2}	0.05–1
ε_{A}	–	1–10	ε_{A}	–	1–10
ε_{B}	–	1–10	d_{P2}	$10^{-3}d$	0–2
d_{A}	$10^{-1}d$	0–2	d_{C}	$10^{-1}d$	0–2
d_{B}	$10^{-1}d$	0–2	d_{P1}	$10^{-3}d$	0–2

Because the number of periodic layers N and the serial number of quasi-periodic layers M are discrete and their values are both integers, the selection of M and N is not included in IPSO, but the two parameters are treated by an exhaustive method: the selection process of these 14 parameters is executed every time M or N changes. This method not only saves on workload of the algorithm but also gives a chance to observe the influence of M and N on the characteristics of absorption.

When the objective function of IPSO is the absolute bandwidth of absorption, the results of absorption for different values of N are shown in Fig. 6. When $N < 4$, it is interesting that the forms of results are very similar. Their absolute bandwidths all come into being at a frequency higher than $3(\omega d/2\pi c)$, and they all have a valley value whose point has a red shift when N increases from 1 to 3 . When $N = 4$, the form of the diagram changes and its absolute bandwidth comes into being at 0.35 to 6.23; the bandwidth shows dramatic growth compared with $N = 1, 2, 3$. The point which should be the valley point in the case of $N = 1, 2, 3$ (point P) rises upon 0.9 and a new valley point appears at 6.4 (point Q). When $N = 5$, the form of the diagram is similar to that of $N = 4$, and the bandwidth rises slightly. When $N = 6$, the form of the absorption diagram returns to that of $N = 1, 2, 3$ and a valley point similar to point Q reappears. When $N = 7$, 8, two types of valley point (P type and Q type) both rise upon 0.9 and the three parts of discontinuous bandwidth become continuous, giving rise to a perfect ultrawide bandwidth. This is complex to express on a physical level but IPSO makes it easy to make out the best combination of all 14 parameters at different values of N and conclude two types of valley point (P type and Q type) together with different forms of diagrams at different values of N.

It is also found that the value of M is not influential on the diagram when $M > 2$. The absorption factor of backward propagating waves stays below 0.1 (shown in Fig. 8), making the bandwidth of nonreciprocal absorption the same as that of the absorption bandwidth of forward propagation. Such satisfactory results in backward propagation are qualitatively owing to the small numerical values of ω_{p2} and ν_2 of the plasma in the quasi-periodic sequence, and the different configuration structures of the forward and backward directions.

When the objective function of IPSO is the relative bandwidth of absorption, the results of absorption for different values of N are shown in Fig. 7. The definition of relative bandwidth is $\mathrm{RBW} = 2(f_{\mathrm{H}} - f_{\mathrm{L}})/(f_{\mathrm{H}} + f_{\mathrm{L}}) = 2(x-1)/(x+1)$, where $x = f_{\mathrm{H}}/f_{\mathrm{L}}$. f_{H} and f_{L} are the upper and lower cutoff frequency respectively. It is evident that relative bandwidth is positively correlated to x, and the most simple way to increase x is to decrease f_{L}, which is why f_{L} of the first absorption band decreases evidently when N rises from 1 to 4. When $N = 5$, it is obvious that f_{L} of the first absorption band is the same but f_{H} of curve of $N = 6$ is higher than that of $N = 5$ and the same thing happens in $N = 7$ and $N = 8$.

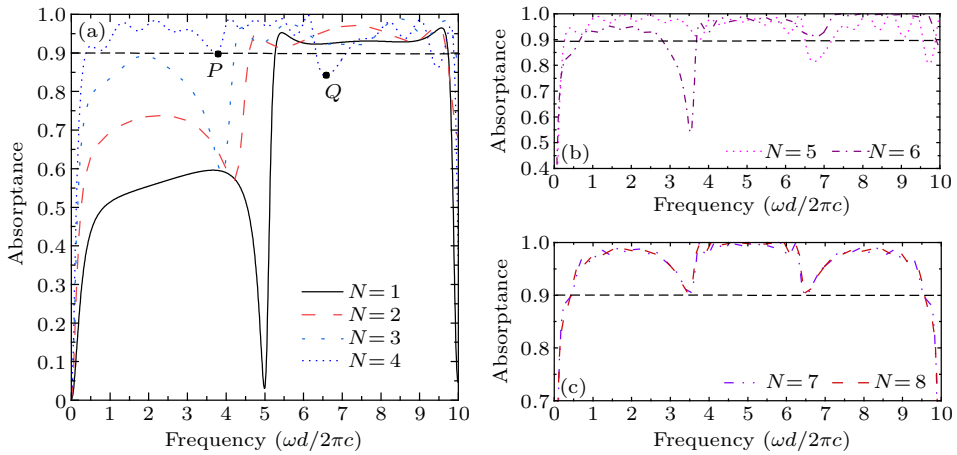

Fig. 6. Results based on IPSO (the objective function is the absolute bandwidth of absorption) when N takes different values. Diagrams of absorptance of forward propagation of $N = 1$, 2, 3, 4 (a), $N = 5$, 6 (b), and $N = 7$, 8 (c). The incident angle is 0°.

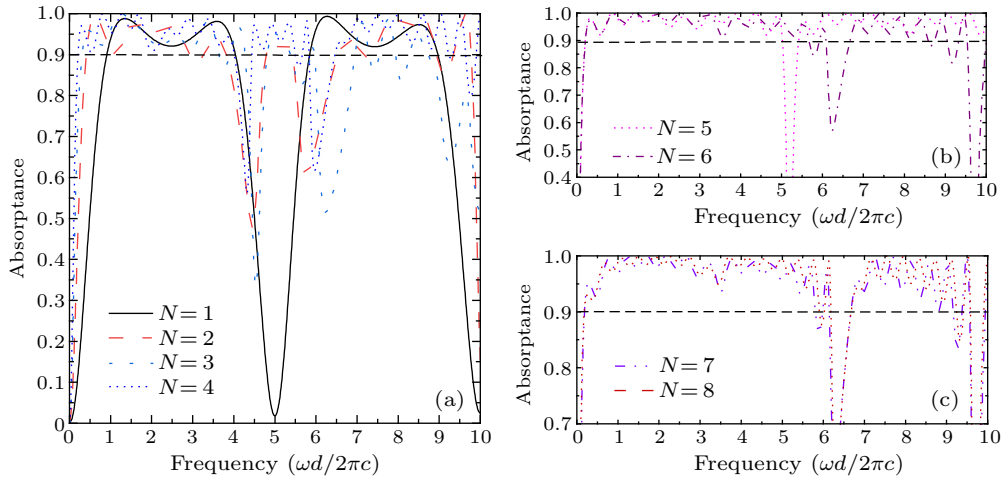

Fig. 7. Results based on IPSO (the objective function is the relative bandwidth of absorption) when N takes different values. Diagrams of absorptance of forward propagation of $N = 1, 2, 3, 4$ (a), $N = 5, 6$ (b), and $N = 7, 8$ (c). The incident angle is 0°.

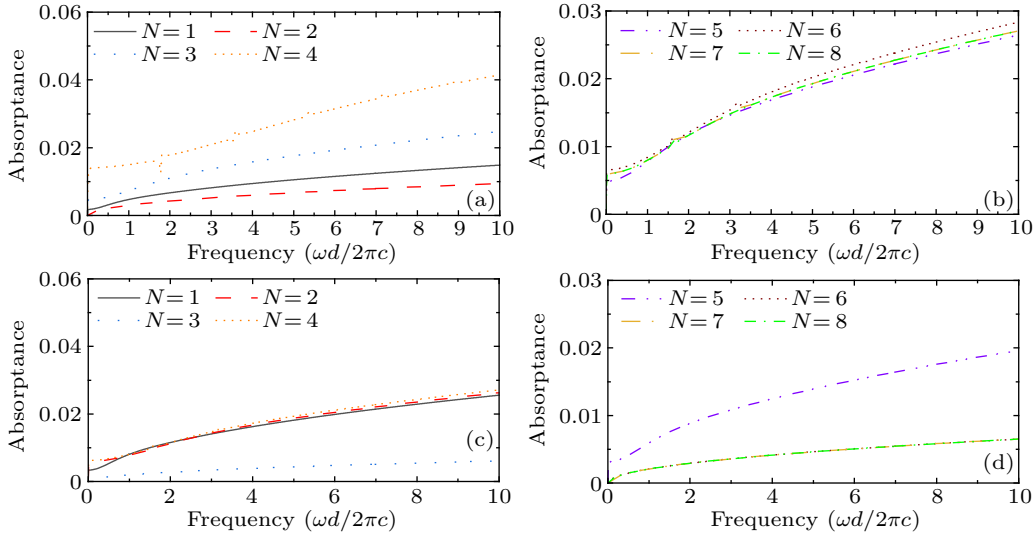

Fig. 8. Diagrams of backward absorptance of (a), (c) $N = 1$–4, (b), (d) $N = 5$–8 when the objective function is (a), (b) absolute bandwidth or (c), (d) relative bandwidth.

3.3. Angular insensitive absorption

To find the probability of angular insensitive absorption, the method of IPSO is taken into account. At this time, the objective function is a dual objective function: angle and bandwidth, which is not as simple as that of ultrawide bandwidth. To mark the difference between TM waves and TE waves, we stipulate that when it is under TM mode, the incident angle is indicated as positive, and when it is under TE mode, the incident angle is indicated as negative.

When bandwidth is attributed more importance, the result is shown in Fig. 9(a). The blue rectangular frame represents the absorption area. In this case, the bandwidth is 9.75 $(\omega d/2\pi c)$ and the absorption angle maximum is 34°. The lower cutoff frequency is 0.25 $(\omega d/2\pi c)$ and the upper cutoff frequency is 10 $(\omega d/2\pi c)$.

When the absorption angle maximum is highlighted, the result is shown in Fig. 9(b). The bandwidth is 5.52 $(\omega d/2\pi c)$ and the absorption angle maximum is 73°. There is also a second choice which is boxed out with a violet rectangular frame in Fig. 9(a). The second choice is not as good as the first choice in bandwidth but is not as bad in angle maximum. Comparing Figs. 8(a) and 9(b), it is found that the margins of the two diagrams are almost the same, the only difference between them being the two fissures that appear in the area under TE mode which are marked off by the dividing line of 0.9 and indicated as fissure$_1$ and fissure$_2$. In Fig. 9(a), the spans on the frequency coordinate of the two fissures are very different (fissure$_1$ is 6.97 $(\omega d/2\pi c)$ and fissure$_2$ is 4.47 $(\omega d/2\pi c)$). However, in Fig. 9(b), the projections of the two fissures on the frequency coordinate are almost the same (fissure$_1$ is 6.38 $(\omega d/2\pi c)$ and fissure$_2$ is 6.20 $(\omega d/2\pi c)$). Comparing the first and second choices, it is evident that a small difference in the projections of fissure$_1$ and fissure$_2$ on the frequency coordinate can lead to larger bandwidth when the angle maximum remains the same. The first choice prevents inefficient bandwidth sacrifice while ensuring a large angle maximum.

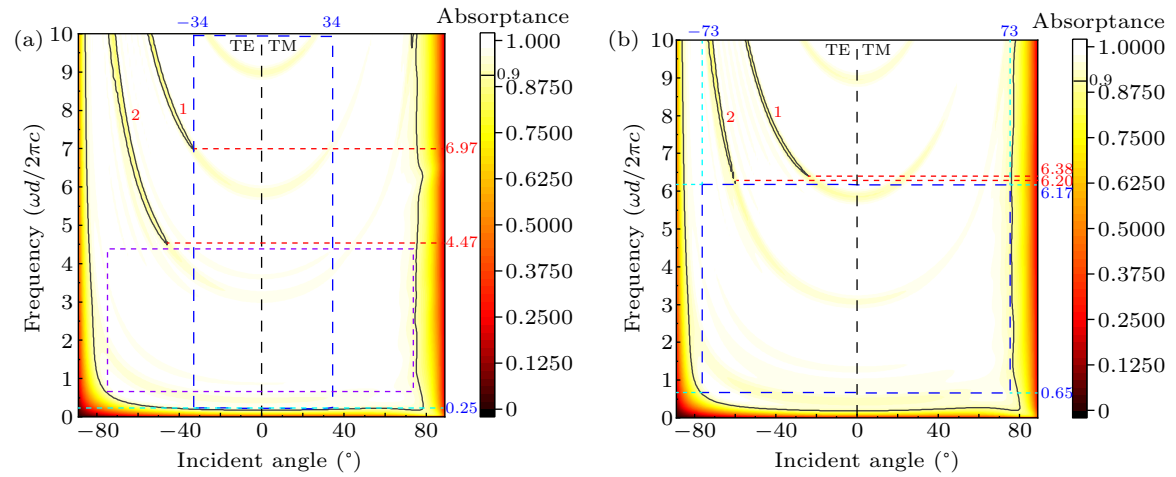

Fig. 9. Results of angular insensitive absorption when (a) bandwidth or (b) angle maximum is attached more importance.

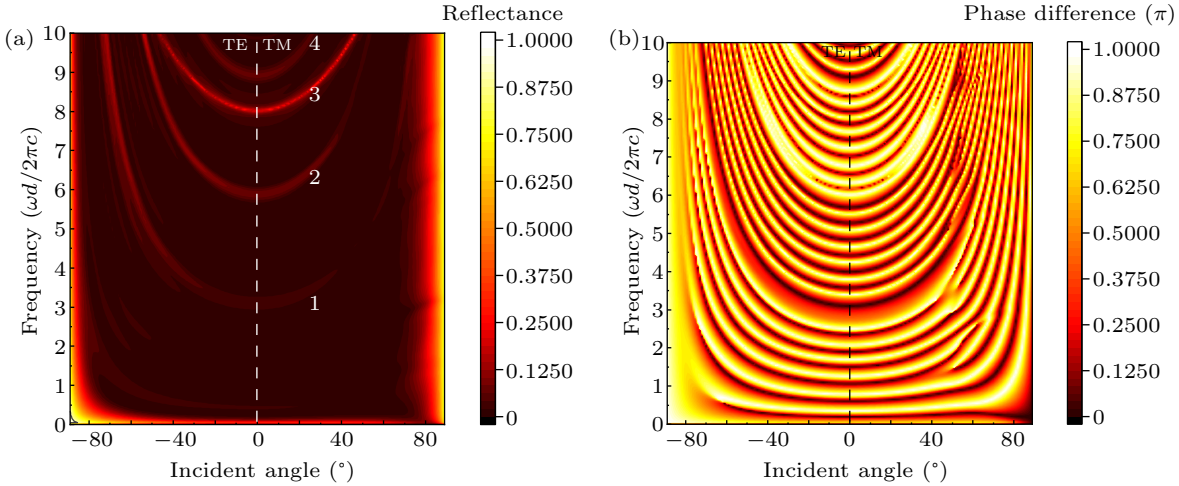

Fig. 10. Comparison of (a) reflectance and (b) phase difference of r.

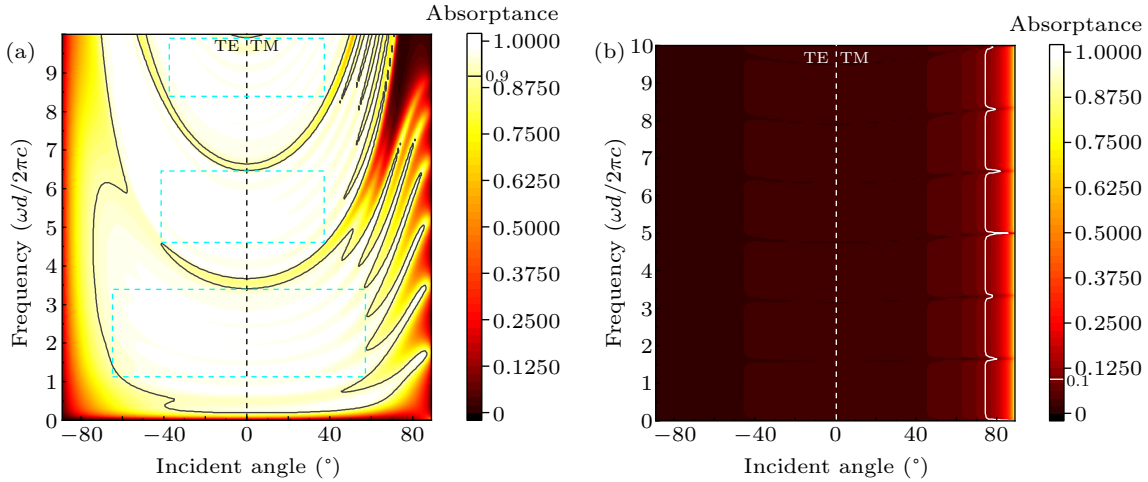

Fig. 11. Nonreciprocal angular insensitive ultrawide bandwidth absorption. Forward (a) and backward (b) absorption of optimized structure.

The mechanism of large angle absorption can be expressed with the interference field theory. The compound amplitude of the reflected magnetic field can be obtained by imposing all kinds of amplitudes of the reflected wave and the transmitted wave. The compound amplitudes of the reflected and transmitted waves' synthetic fields are worked out as

$$A^{(\mathrm{r})} = \frac{\left(1 - \mathrm{e}^{\mathrm{i}\delta_{\mathrm{r}}}\right)\sqrt{R}}{1 - R \cdot \mathrm{e}^{\mathrm{i}\delta_{\mathrm{r}}}} \cdot A^{(\mathrm{i})},$$

$$A^{(\mathrm{t})} = \frac{T}{1 - R \cdot \mathrm{e}^{\mathrm{i}\delta_{\mathrm{t}}}} \cdot A^{(\mathrm{i})}. \tag{16}$$

Take reflectance, for instance; when δ_r is an even multiple of $\pi/2$, the reflected wave satisfies the interference cancelation condition, which gives rise to the lowest reflection and energy gathering within the structure and transmission. An excellently low reflection area and its corresponding phase difference are shown in Fig. 10. Reflectance is perfectly low except for four macroscopical flaws and their locations at 0° are 3.1 to 3.5, 6.0 to 6.25, 8.1 to 8.2, and 9.0 to 9.2 respectively (numbered $\text{flaw}_{1,2,3,4}$). Phase differences step on 0π and 1π, and seldom stay on other values between 0 and 1. This satisfies the interference cancelation and generates perfectly low reflectance. At the positions of these four flaws, the phase differences all make a short stay between 0 and $1(\pi)$, disobeying the interference cancelation theory. It is also seen that flaw_1 and flaw_2 disappear under TM mode. This is reflected in Fig. 11(b) in which areas where the phase difference stays between 0 and $1(\pi)$ become narrow under TM mode.

3.4. Nonreciprocal angular insensitive ultra wide bandwidth absorption

The physical properties of plasma provide the structure with good nonreciprocal absorbing ability. Utilizing IPSO, a structure supporting nonreciprocal angular insensitive ultrawide bandwidth absorption (NAIB) (absorption from forward propagation is above 0.9 and that from backward propagation is below 0.1) is obtained; details are shown in Fig. 11.

The overlapping absorptance areas of Figs. 11(a) and 11(b), the NAIB areas, are shown in Fig. 10(a) in the blue rectangular frame. There are three NAIB areas. Their bandwidths are 2.1, 2.02, and 1.98 and their respective maximum angles are 58°, 40°, and 36°. The area in which absorptance from backward propagation is below 0.1 is quite large: the total area in TE mode and the area from 0° to 75° in TM mode. That means the NAIB area is determined by absorption from forward propagation, especially when the incident angle is between 0° and 75° under TM mode. In Fig. 11(a), it is found that the absorption area for which the incident angle is below 75° under TM mode is quite broad while many flaws appear when the incident angle increases above 75° under TM mode. This phenomenon from forward propagation caters to the condition that the area for which the incident angle is above 75° under TM mode does not satisfy the term that absorptance is below 0.1.

3.5. Influence of M

In Fig. 12, we find that the absorption area stretches from left to right with increasing M. It is discussed that M is not as decisive to absorption bandwidth when the incident angle is 0°, but crucial to absorption when the incident angle grows from zero. An absorption area always exists at large incident angles under TE mode and the absorption area slowly extends to the area of TM. We can draw a line to describe the stretching of the absorption area which is presented with red lineation. The position of the line is -68 ($M=2$), -52 ($M=3$), 49 ($M=4$), 78 ($M=5$) (unit: $(\omega d/2\pi c)$).

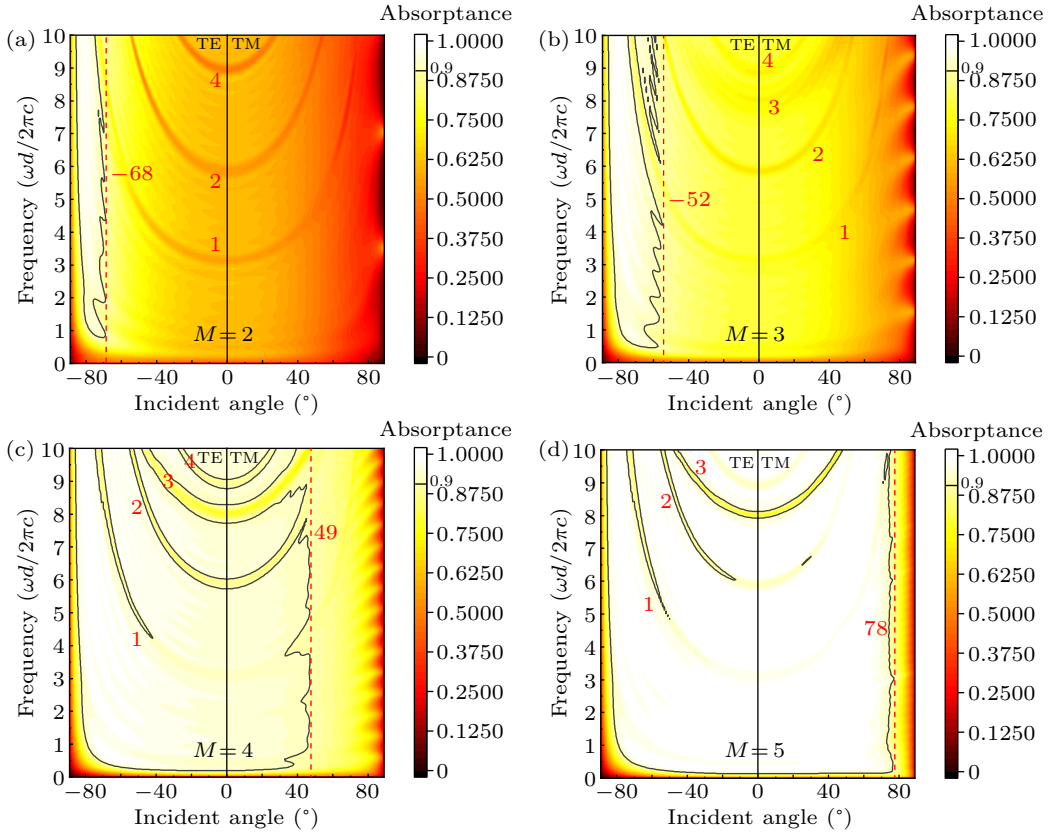

Fig. 12. Diagrams of absorptance of (a) $M=2$, (b) $M=3$, (c) $M=4$, (d) $M=5$.

Observing Figs. 12(a)–12(d), it is concluded that there are four kind of fissures which are marked out as fissure$_{1,2,3,4}$ in red. Fissures 1, 2, 3, and 4 are classified by their position on the axis for which the incident angle is 0°. Their positions are respectively 3.1, 5.9, 7.9, and 8.9 (in units of $(\omega d/2\pi c)$). When $M = 2$, fissure$_{1,2,4}$ can be seen. When $M = 3$, fissure$_{1,2,3,4}$ appear faintly. When $M = 4$, it is obvious that fissure$_{1,2,3,4}$ become visible and the area near them satisfies the condition that absorptance is higher than 0.9. When $M = 5$, fissure$_4$ become invisible and the other fissures gradually retreat, and the absorption area slowly becomes rather broad without fissures.

3.6. Influence of ν_1

Different diagrams with different ν_1 are shown in Fig. 13. The absorption area exists stably regardless of the value of ν_1 at large incident angles under TM mode and stretches towards small incident angles under TM mode and TE mode. In this case, there are three annular cracks evenly distributed at 3, 6, and 9 (in units of $(\omega d/2\pi c)$). The absorptance of these three cracks stands in stark contrast to that of their surrounding area when $\nu_1 = 0.05$. This contrast gradually fades away when ν_1 increases and the absorption area slowly submerges in the vicinity of these three cracks. The sharp contrast of the cracks to their adjacent area stays phanic until ν_1 increases to 0.24.

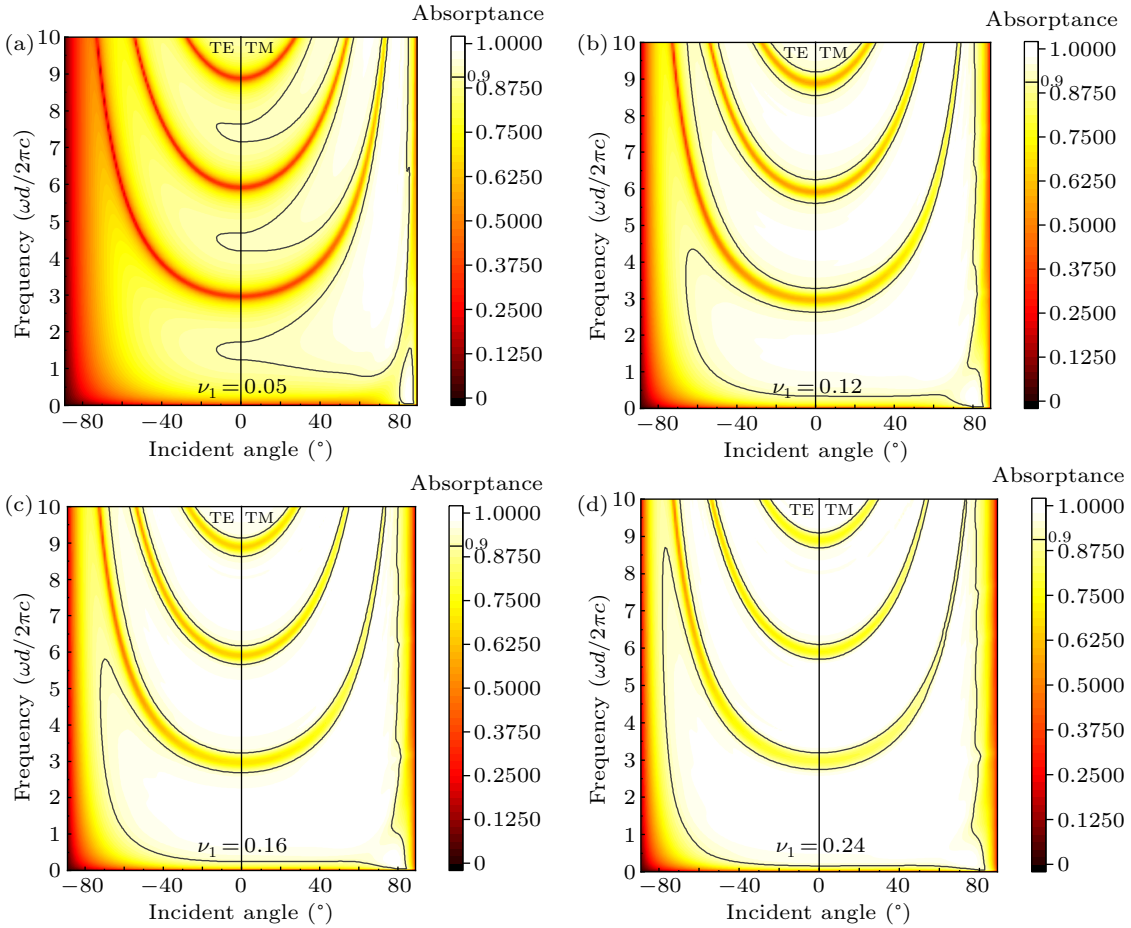

Fig. 13. Diagrams of absorptance of (a) $\nu_1 = 0.05$, (b) $\nu_1 = 0.12$, (c) $\nu_1 = 0.16$, (d) $\nu_1 = 0.24$.

4. Conclusion

In summary, this paper investigates a nonreciprocal ultrawide band absorber with excellent angular insensitivity arranged by a cascading structure composed of a periodic sequence and Octonacci sequence which are made of conventional dielectrics and plasma sheets. The great capacity of nonreciprocal large angle absorption can be attributed to the specific sequence of the structure and fine characteristic of the plasma, which make it possible for IPSO to find the most satisfactory optimal solution of 14 parameters to be optimized. There is also a clear division of labor of N and M in which N is responsible for ultrawide band absorption and M affects angular sensitivity, especially under TM mode. When absolute and relative bandwidth are set as the objective function respectively, the results of absorption from forward and backward prpopagation are discussed. Nonreciprocal angular insensitive ultrawide bandwidth absorption is realized. Angle-bandwidth (bandwidth priority) is $34° - 9.75\ \omega d/2\pi c$. Angle-bandwidth (angle priority) is $73° - 5.52\ \omega d/2\pi c$. The influences of cyclotron frequency ν_1 and M are also surveyed. These two

parameters can tune the whole absorption characteristic diagram from two different ways so that they can realize almost complete tuning of absorption under both TE and TM mode. We believe this kind of nonreciprocal ultrawide band angular insensitive absorber has great potential for optoelectronic devices and IPSO can play a role in optimization problems in PC fields.

References

[1] Yablonovitch E 1987 *Phys. Rev. Lett.* **58** 2059
[2] John S 1987 *Phys. Rev. Lett.* **58** 2486
[3] Kim S H, Kim S and Kee C S 2016 *Phys. Rev. B* **94** 085118
[4] Meng F, Li Y, Li S, Lin H, Jia B and Huang X 2017 *J. Lightw. Technol.* **35** 1670
[5] Aly A H, Sayed F A and Elsayed H A 2020 *Appl. Opt.* **59** 4796
[6] Avendano C and Reyes A 2017 *Liq. Cryst.* **44** 1620
[7] McGurn A.R. 1999 *Phys. Lett. A* **251** 322
[8] Chen S, Yang X, Meng X, Dong G, Wang Y, Wang L and Huang Z 2013 *Chin. Phys. Lett.* **30** 054206
[9] Georgaki M I, Botsialas A, Argitis P, Papanikolaou N, Oikonomou P, Raptis I, Rysz J, Budkowski A and Chatzichristidi M 2014 *Microelectron. Eng.* **115** 55
[10] Beiu R M, Beiu V and Duma V F 2017 *Opt. Express* **25** 23388
[11] Lin W H, Wu C J, Yang T J and Chang S J 2010 *Opt. Express* **18** 27155
[12] Lee H and Wu J 2010 *J. Appl. Phys.* **107** 09E149
[13] Liu Y, Zhong R, Huang J, Lv Y, Han C and Liu S 2019 *Opt. Express* **27** 7393
[14] Cai Y and Xu K 2018 *Opt. Express* **26** 31693
[15] He S and Chen T 2013 *IEEE Trans. Terahertz Sci. Technol.* **3** 757
[16] Wu C, Yang T, Li C and Wu P 2012 *Prog. Electromagn. Res.* **126** 521
[17] Tan H, Jin C, Zhuge L and Wu X 2019 *IEEE Trans. Plasma Sci* **47** 3986
[18] Hojo H and Mase A 2004 *J. Plasma Fusion Res.* **80** 89
[19] Dong H, Wang J and Fung K 2013 *Opt. Lett.* **38** 5232
[20] Ma Y, Zhang H, Liu T and Li W 2019 *J. Opt. Soc. Amer:. B, Opt. Phys.* **36** 2250
[21] Zhang J and Benson T M 2013 *J. Mod. Opt.* **60** 1804
[22] Fang Y, Wang Y and Xia J 2019 *Acta Phys. Sin.* **68** 194201 (in Chinese)
[23] Amel L and Abdelmadjid B 2015 *Chin. Phys. Lett.* **32** 54204
[24] Li Q, Wu R, Yang Y and Sun H 2013 *Chin. Phys. Lett.* **30** 074208
[25] Chen Y, Zhu J, Xie Y, Feng N and Liu Q 2019 *Nanoscale* **11** 9749
[26] Kennedy J and Eberhart R 1995 *Proc. IEEE Int. Conf. on Neural Networks*, November 27, 1995–December 1, 1995, Perth, WA, Australia, p. 1942
[27] Shi Y and Eberhart R 1998 *Proc. IEEE Int. Conf. on Evolutionary Computation*, May 4–9, 1998, Anchorage, AK, USA, pp. 69–73
[28] Farnad B, Jafarian A and Baleanu D 2018 *Appl. Math. Model.* **55** 652
[29] Liu D and Sen H 2019 *Acta Phys. Sin.* **68** 024206 (in Chinese)
[30] Ginzberg V L 1970 *The Propagation of Electromagnetic Waves in Plasmas* (New York: Pergamon Press)
[31] Qi L, Yang Z, Lan F, Gao X and Shi Z 2010 *Phys. Plasmas* **17** 042501